

Processability of A6061 Aluminum Alloy Using Laser Powder Bed Fusion by In Situ Synthesis of Grain Refiners

*Original*

Processability of A6061 Aluminum Alloy Using Laser Powder Bed Fusion by In Situ Synthesis of Grain Refiners / Rosito, Michele; Vanzetti, Matteo; Padovano, Elisa; Gili, Flavia; Sampieri, Roberta; Bondioli, Federica; Badini, Claudio Francesco. - In: METALS. - ISSN 2075-4701. - ELETTRONICO. - 13:6(2023). [10.3390/met13061128]

*Availability:*

This version is available at: 11583/2979524 since: 2023-06-23T07:55:38Z

*Publisher:*

MDPI

*Published*

DOI:10.3390/met13061128

*Terms of use:*

This article is made available under terms and conditions as specified in the corresponding bibliographic description in the repository

*Publisher copyright*

(Article begins on next page)

## Article

# Processability of A6061 Aluminum Alloy Using Laser Powder Bed Fusion by In Situ Synthesis of Grain Refiners

Michele Rosito <sup>1,\*</sup> , Matteo Vanzetti <sup>1,2</sup> , Elisa Padovano <sup>1</sup>, Flavia Gili <sup>3</sup>, Roberta Sampieri <sup>4</sup>, Federica Bondioli <sup>1,5</sup>  and Claudio Francesco Badini <sup>1</sup>

<sup>1</sup> Department of Applied Science and Technology, Politecnico di Torino, Corso Duca degli Abruzzi 24, 10129 Turin, Italy; matteo.vanzetti@polito.it (M.V.); elisa.padovano@polito.it (E.P.); federica.bondioli@polito.it (F.B.); claudio.badini@polito.it (C.F.B.)

<sup>2</sup> Center for Sustainable Future Technologies IIT@Polito, Istituto Italiano di Tecnologia, Via Livorno 60, 10124 Torino, Italy

<sup>3</sup> Centro Ricerche Fiat S.c.p.A. (CRF) Stellantis, Corso Settembrini 40, Corpo 1, Ingresso 109/A, 10135 Torino, Italy; flavia.gili@crf.it

<sup>4</sup> Stellantis, Via Biscaretti di Ruffia 90/A, 10135 Torino, Italy; roberta.sampieri@stellantis.com

<sup>5</sup> Consorzio Interuniversitario Nazionale per la Scienza e Tecnologia dei Materiali (INSTM), Via G. Giusti 9, 50121 Firenze, Italy

\* Correspondence: michele.rosito@polito.it

**Abstract:** Despite the increasing interest in laser powder bed fusion (LPBF), only a few cast aluminum alloys are available for this process. This study focuses on improving the LPBF processability of the A6061 alloy, which is challenging due to its wide solidification range, the dendritic columnar grain growth, and consequent solidification cracking. To address these issues, in situ-synthesized grain refiners can be used to induce equiaxial grain growth and prevent crack formation. A6061 RAM2 powder—a mixture of A6061, Ti, and B<sub>4</sub>C—was characterized and processed using a low-power LPBF machine to create an in situ particle-reinforced metal matrix composite. Parameter optimization was performed to evaluate the effect of their variation on the printability of the alloy. Microstructural characterization of the samples revealed that the complete reaction and the synthesis of the ceramic reinforcement did not occur. However, TiAl<sub>3</sub> was synthesized during the process and promoted a partial grain refinement, leading to the formation of equiaxial grains and preventing the formation of solidification cracks. The tensile tests carried out on the optimized samples exhibit superior mechanical properties compared to those of A6061 processed through LPBF.

**Keywords:** LPBF; modified A6061; metal matrix composite; in situ grain refiners; reactive additive manufacturing; TiAl<sub>n</sub>



**Citation:** Rosito, M.; Vanzetti, M.; Padovano, E.; Gili, F.; Sampieri, R.; Bondioli, F.; Badini, C.F. Processability of A6061 Aluminum Alloy Using Laser Powder Bed Fusion by In Situ Synthesis of Grain Refiners. *Metals* **2023**, *13*, 1128. <https://doi.org/10.3390/met13061128>

Academic Editor: Chenglong Ma

Received: 15 May 2023

Revised: 9 June 2023

Accepted: 14 June 2023

Published: 16 June 2023



**Copyright:** © 2023 by the authors. Licensee MDPI, Basel, Switzerland. This article is an open access article distributed under the terms and conditions of the Creative Commons Attribution (CC BY) license (<https://creativecommons.org/licenses/by/4.0/>).

## 1. Introduction

In recent decades, the interest of the scientific community in laser powder bed fusion (LPBF) has grown exponentially. This additive manufacturing technology, also known as selective laser melting (SLM), can produce metal parts using a layer-by-layer strategy. The additive approach offers many advantages [1]; in fact, it can (i) obtain near-net shape parts with complex geometries and lightened structures; (ii) optimize the use of the material reducing the production of waste; and (iii) fabricate parts with particular microstructures and improved mechanical properties due to the high cooling rate involved in the process [2,3]. Due to its ability to fabricate components with high performance and efficiency, LPBF is used in different application fields such as aerospace, automotive, and biomedical [4,5].

The great interest and the widespread use of Al alloys in various industrial sectors have induced many researchers to study their processability by LPBF [6]. Al alloys are characterized by a relatively low cost, low density, high specific strength, and high oxidation resistance. Currently, the number of Al alloys which can be effectively processed by LPBF is

limited. In fact, their printability is affected by several features such as high reflectivity, high thermal conductivity, and poor flowability of the powder [7]. Among traditional Al alloys, near-eutectic cast alloys such as AlSi10Mg [8–13], AlSi12 [14,15], and A357 [16–18] are the most studied and suitable for LPBF [2]. This is due to the high Si content, which improves both the processability and the printability of these alloys by enhancing the fluidity of the melted alloy, narrowing the solidification range [19], and increasing the fraction of absorbed energy [2]. As proved by the high number of published works, significant improvements have been achieved in the processing of Al cast alloys by LPBF. However, further efforts are needed to promote their uptake by industry [6].

The increasing interest in the development of new Al-based systems to overcome the difficulties in processing these kinds of alloys by LPBF is the main reason for studying the suitability of traditional Al wrought alloys, especially high-strength Al alloys such as 2000, 5000, 6000, and 7000 series, for LPBF technology [20]. These alloys are commonly used in aerospace and automotive fields because of their improved mechanical properties. However, these materials have poor processability by LPBF due to their wide solidification range, poor fluidity, and, consequently, high crack susceptibility [21]. In fact, these alloys solidify with dendritic growth, creating interdendritic; because of the development of local stresses resulting from solidification, cracks can propagate along interdendritic directions [22]. Solidification cracking is, in fact, observed to be the main issue that affects the processability of these alloys. Maamoun et al. [23] studied the effect of LPBF process parameters on the microstructure of both AlSi10Mg and Al6061 parts, and they found a high crack density in their Al6061 samples. Furthermore, it was observed that process parameters can only limit the size of cracks but not eliminate them. Another important issue is the presence of volatile alloying elements such as Zn, Mg, and Li which may evaporate due to the high energy density used during the process. This may cause modification in the alloy composition, leading to an inhomogeneous chemical composition of the part, compromising the beneficial effects of following precipitation heat treatment. In their work, Aboulkhair et al. [13] observed the depletion of Mg in printed AlSi10Mg parts when compared to the virgin powder, supposing that it could depend on the evaporation and the scattering of this element. Li et al. [24] investigated the influence of energy density on various properties of as-built 7075 aluminum alloy. The authors observed a linear relationship between the volumetric energy density (VED) and the loss in weight of low-melting alloying elements such as Zn and Mg. Additionally, despite the optimization of process parameters resulting in near-fully dense samples (99.4%), solidification cracks were observed in the optimized LPBF-processed samples.

In recent years, researchers have focused their efforts on overcoming these issues to improve the printability of these alloys and make them available for industrial use. To the authors' knowledge, three different approaches have been used and described in the literature. The first one involves modifying the chemical composition of the alloy by increasing the Si content. A higher Si content can narrow the solidification range and increase the fluidity of the molten metal. Hyer et al. [25] investigated the role of Si in mitigating hot cracking susceptibility in aluminum alloys. Six binary Al-Si alloys with different compositions (ranging from 0.5 to 16 wt.% Si) were characterized in terms of density, microstructure, and mechanical properties. The study revealed that alloys with lower Si content exhibited micro-cracks, whereas increasing the Si content prevented the occurrence of solidification cracks. Montero-Sistiaga et al. [26] obtained dense (99%) and crack-free Al7075 samples by mixing Si and Al7075 powders, with mechanical properties comparable to those of the traditional alloy. Increasing the Si content (from 1 to 4 wt.%) led to a decrease in crack density and significant grain refinement. The second approach consists of applying a high-temperature preheating of the building platform to mitigate thermal stress. Uddin et al. [27] used an induction heater to heat the platform to 350–500 °C and obtained fully dense (>98%), crack-free, and pure Al6061 samples. However, the high temperature of the building platform was observed to induce the formation of incoherent precipitates and alter the typical LPBF microstructure.

The third method involves the introduction of nucleants into the system: the presence of nucleation sites in the alloy induces a columnar-to-equiaxed microstructural transition and promotes the growth of equiaxed grains, thus avoiding cracks development. Martin et al. [22] modified Al7075 and Al6061 powders by coating the particles with hydrogen-stabilized zirconium, while Mehta et al. [28] mixed Al6061 powder with Zr powders. Both studies observed the nucleation of fine Al<sub>3</sub>Zr particles during the process, which acted as heterogeneous nucleation sites and promoted the formation of equiaxed and fine grains. Dense and crack-free samples were obtained and observed in both studies. Therefore, the production of aluminum matrix composites (AMCs) can be a valid approach to enhancing the printability of high-strength aluminum alloys and improving their mechanical properties.

Al6061 is one of the most interesting high-strength Al alloys for industrial applications due to its lightness, high strength, excellent formability, and good corrosion resistance. It is an Al-Mg-Si alloy, and it can be heat treated for precipitation strengthening. Researchers have made significant efforts in recent years to make it printable and processable by LPBF. In addition to the previously discussed strategies, reactive additive manufacturing (RAM) is going to be considered a valid approach for high-strength Al alloys. This patented technology [29] involves the use of a metal powder mixed with different components that can react and form ceramic reinforcement phases. These phases act as grain refiners and heterogeneous nucleation sites, enabling the processability of high-strength Al alloys. A new printable Al6061 RAM alloy for LPBF has recently been made available on the market. However, despite the great potential of this material to produce crack-free Al6061 parts using the AM technique, to the authors' knowledge only a few papers on this topic have been published [30–32]. Moreover, in these studies, information regarding the powder formulation, and LPBF process conditions including process parameters are not provided because of the collaboration with the supplier company and the patent.

In this work, the A6061 RAM2 system was characterized in terms of powder feedstock and LPBF process. The optimization of process parameters was performed on the material processed by a low-power LPBF machine. The effect of power laser, scanning speed, and volumetric energy density on the printability of the alloy was evaluated. The reaction mechanism and the evolution of the microstructure were also investigated. Finally, after identifying the optimized parameter set for high density, the mechanical properties of the processed material were evaluated through tensile tests, comparing the results with pure A6061 processed by LPBF.

## 2. Materials and Methods

### 2.1. Powder Characterization

A6061 RAM2 powder, supplied by Elementum 3D (Erie, CO, USA) was used for this study. Because of the patented technology and the lack of information from the supplier, a complete powder characterization was performed to investigate the powder's composition and properties. Powder density was evaluated using a Helium Pycnometer Ultrapyc 5000 (Anton Paar GmbH, Graz, Austria), and an elemental analysis to evaluate the content of C in the powder was performed using a carbon and sulfur Combustion Analyzer CS744 Series (LECO Corporation, St. Joseph, MI, USA). The particle size distribution of the powder was carried out using a laser diffraction particle size analyzer Mastersizer 3000 (Malvern Panalytical, Malvern, UK). Powder micrographs were acquired with a Zeiss FE-SEM Merlin (Zeiss, Oberkochen, Germany), while the phase identification was performed with a PANalytical Empyrean diffractometer (Malvern Panalytical, Malvern, UK). The XRD analysis of the powder was carried out using a Bragg–Brentano geometry and Cu K $\alpha$  radiation at 40 kV and 40 mA. The powder sample was investigated in a 2 $\theta$  range between 30° and 110°, with a step size of 0.013°/s and a time step of 60 s.

Before printing, the powder was sieved under 50  $\mu$ m and dried for 2 h at 90 °C to eliminate moisture, thus preventing hydrogen porosity [33] and improving the flowability [34].

## 2.2. LPBF Process

Massive samples were produced using a Concept Laser Mlab Cusing R (General Electric, Boston, MA, USA), an LPBF machine with a small build volume (building platform  $90 \times 90 \text{ mm}^2$ , building height 8 cm), equipped with a 100 W fiber laser emitting at a wavelength of 1070 nm and a spot size of 50  $\mu\text{m}$ .

A total of three jobs were manufactured. The first two jobs were carried out to optimize the process parameters. Sixteen cubic samples ( $10 \times 10 \times 10.5 \text{ mm}^3$ ) were produced for each job, resulting in a total of 32 cubic specimens. Aluminum platforms were used as substrate. All samples were printed with a layer thickness ( $t$ ) of 15  $\mu\text{m}$  and a hatching distance ( $h$ ) of 100  $\mu\text{m}$ . The laser power ( $P$ ) varied within the range of 80 to 95 W, while the investigated volumetric energy density (VED) ranged from 60 to 130  $\text{J}/\text{mm}^3$ . The process parameters used in this study were chosen based on a preliminary review of the literature focused on the processing of A6061 alloy [35] and other aluminum alloys [36,37] using LPBF machines with similar maximum laser power. The range of VED investigated was expanded to account for the exothermic phenomena that occur during the reaction mechanism. The scanning speed ( $v$ ) for the adopted process parameters was calculated using Equation (1), while keeping the other parameters constant, and ranged from 390 to 1000 mm/s. A summary of the process parameters is given in Table 1.

$$\text{VED} = \frac{P}{t \times h \times v} \quad (1)$$

**Table 1.** Process parameters used for jobs 1 and 2.

Volumetric Energy Density ( $\text{J}/\text{mm}^3$ )	Scanning Speed (mm/s)			
	Power 80 W	Power 85 W	Power 90 W	Power 95 W
60	847	899	952	1005
70	726	771	816	862
80	635	675	714	754
90	564	600	635	670
100	508	540	571	603
110	462	491	519	548
120	423	450	476	503
130	391	415	440	464

Lastly, a third job was manufactured with a set of optimized parameters to evaluate the mechanical properties of the printed material. This last job consisted of 6 dog bone specimens built horizontally according to ASTM E8/E8M-22 [38], with the longitudinal axis aligned parallel to the platform.

## 2.3. Characterization of the Bulk Samples

A6061 RAM2 samples were removed from the platform using an electrical discharge machine (EDM). Cubic specimens were coarsely polished to eliminate the surface roughness and their densities were evaluated with pycnometer measurements (density measurements were also made by Archimedes' method to confirm those made with the pycnometer). The optimized set of parameters for the third job was chosen on the basis of the obtained density values.

All the cubic samples were cut along the building direction, mounted, polished, and etched with Kroll reactant for 40 s to observe the microstructure. Micrographs across the building direction were acquired with both Leica DMI 5000 M optical microscope (Leica Microsystems, Wetzlar, Germany) and Phenom ProX SEM (Thermo Fisher Scientific, Waltham, MA, USA) equipped with an EDS detector. Moreover, portions of the cubic

samples were cut and prepared to perform XRD analysis for phase identification. XRD measurements were conducted similarly to that carried out on the powder.

At last, the mechanical properties of the bulk material were evaluated. Six dog bone specimens printed using the optimized process parameters set were tested using a tensile machine Zwick/Roell ProLine Z050 Universal (Zwick Roell Group, Ulm, Germany) using a strain rate of  $8 \times 10^{-3} \text{ s}^{-1}$ . A strain gauge (with an initial length of 10 mm and placed in the middle of the gauge length) was used to measure the strain. Young's modulus and yield stress were estimated according to the BS EN ISO 6892-1:2019 standard [39].

### 3. Results and Discussion

#### 3.1. Powder Characterization

The density of the powder was measured with a helium pycnometer, and it was evaluated at  $2.7574 \pm 0.0011 \text{ g/cm}^3$ . In Figure 1, both relative and cumulative particle size distributions of A6061 RAM2 powder are shown. The relative curve displays a monomodal distribution. As reported in Figure 1,  $D_{50}$  and  $D_{90}$  values comply with those of other powders for LPBF [40], while the  $D_{10}$  value is lower, indicating a higher fraction of fine particles. In fact, a low-intensity peak evidences the presence of a not negligible amount of fine particles with dimensions in a range from 3 to 10  $\mu\text{m}$ . These may correspond to the precursors of ceramic reinforcements added to the Al-based alloy. It is well known that the size of reinforcement is one of the main factors that influence the in situ reaction. Chang et al. [41] studied the effect of starting SiC particle size on the processing of  $(\text{Al}_4\text{SiC}_4 + \text{SiC})/\text{Al}$  hybrid composites produced by selective laser melting. The experimental results showed that the use of SiC particles with  $D_{50}$  of 5  $\mu\text{m}$  allows us to obtain the highest density if compared to those obtained with the addition of SiC particles with  $D_{50}$  of 15  $\mu\text{m}$  and 50  $\mu\text{m}$ , respectively. In fact, when SiC particle size decreased, the in situ reaction between the aluminum matrix and SiC was enhanced and, accordingly, a higher amount of the  $\text{Al}_4\text{SiC}_4$  reaction product was observed.

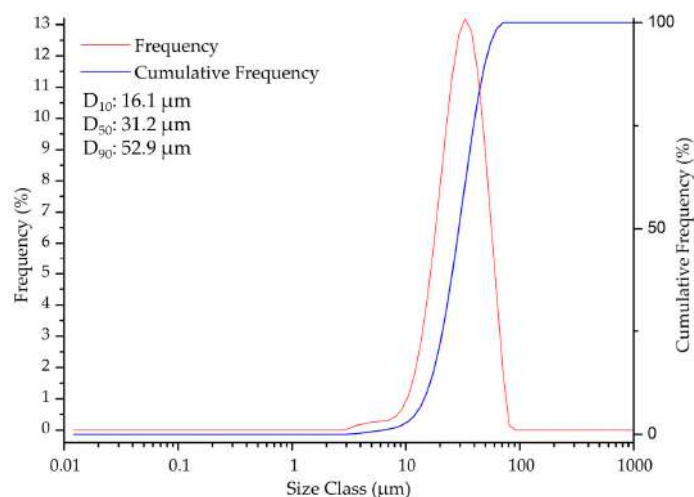


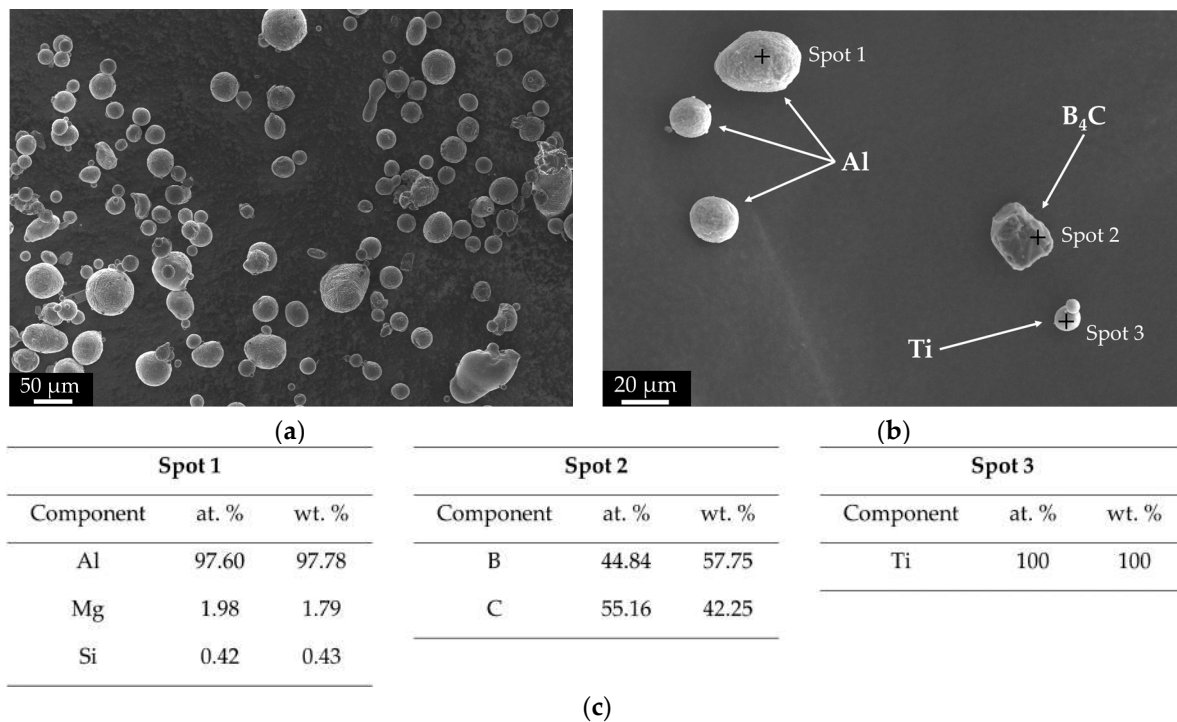
**Figure 1.** A6061 RAM2's particle size distribution, where is reported the relative distribution (red line) and the cumulative one (blue line).

Moreover, with reference to in situ production of composites by additive manufacturing technologies, it was found that the laser absorptivity increases with decreasing powder particle size. In fact, Gu et al. [42] reported that the addition of SiC and  $\text{TiB}_2$  particles with a dimension of about 5  $\mu\text{m}$  enhanced the absorptivity of the  $\text{AlSi10Mg}$  matrix.

Figure 2a shows A6061 RAM2 powder which, as expected, consists of three components, mixed in a reactive formulation. In Figure 2b the three reactants can be recognized, due to the different morphology and dimension; further, EDS analyses performed on the different particles (whose results are reported in Figure 2c) highlighted chemical differences and made it possible to identify them. Al particles are the main component in the system,



and they are characterized by higher dimensions, rough surfaces, and approximately spherical shapes. The EDS analysis conducted on these particles revealed the presence of Mg and Si as the primary alloying elements, thus confirming a composition consistent with A6061. Titanium particles are the second component, and they are identifiable by smaller dimensions and a more regular spherical morphology. Finally, carbon boride particles have an irregular and polygonal shape. EDS analysis confirmed the presence of B and C. However, it is not possible to determine the stoichiometric ratio between B and C. EDS is, in fact, a semiquantitative analysis, and the determination of light elements such as C, B, and N is not accurate [43].



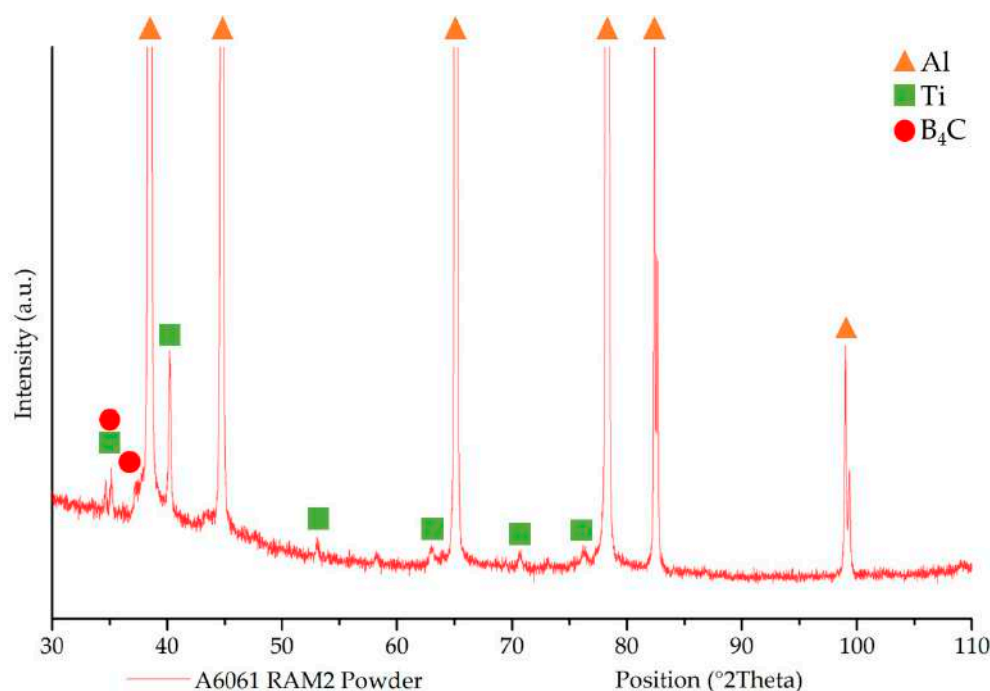
**Figure 2.** SEM images of A6061 RAM2 powder at (a) lower and (b) higher magnification. (c) EDS analysis performed on the particles.

Figure 3 shows the XRD analysis performed on the powder which confirmed the presence of these three components, although the peaks attributed to Ti and  $B_4C$  have low intensity if compared to Al peaks. The low intensity of the peaks belonging to the precursors suggests that these are added to the system in a small amount with respect to A6061. According to the information provided by the supplier, the amount of ceramic reinforcement in the printed material should constitute 2% volume. As explained in detail in the following paragraph, the precursors are expected to undergo a complete reaction to produce the reinforcing phases. Therefore, their amount in the powder would fall within the range of 2–3% [44].

### 3.2. A6061 RAM2 System

As discussed previously, reactive additive manufacturing is a technology patented by Elementum 3D that combines the processes of LPBF and self-sustaining high-temperature synthesis (SHS) process. It is used for the production of a metal matrix composite, combining additive manufacturing and in situ reactions. The powder used in the LPBF process is a mix of several components able to react with each other thanks to the laser, which triggers a sequence of reactions supplying energy to the system. These reactions play a crucial role in the reinforcement formation and the energy system. On one hand, they involve the synthesis of the ceramic reinforcement with a strong interfacial bond due to the in situ

formation [45]. On the other hand, the reactions are exothermic, and the released energy can assist the LPBF process.



**Figure 3.** A6061 RAM2 powder's low-intensity XRD pattern.

Powder characterization of the A6061 RAM2 system made it possible to recognize the components as Al alloy, Ti, and B<sub>4</sub>C particles. This system was investigated by Shen et al. [46] to produce in situ Al/TiC-TiB<sub>2</sub> composites and the following reaction mechanism was proposed.

The first step involves the melting of the Al matrix, followed by its reaction with Ti particles to form TiAl<sub>n</sub>, according to Equation (2).



The synthesis of these intermetallics has a key role in the formation of the ceramic TiC and TiB<sub>2</sub> reinforcement. In fact, TiAl<sub>n</sub> surrounds carbon boride particles because of the convective motives induced by the laser. The formation of the TiAl<sub>n</sub>/B<sub>4</sub>C interfaces promotes the interaction between Ti, C, and B and the subsequent reactions, reducing the atomic diffusion distance. At the same time, the formation of TiAl<sub>n</sub> is exothermic, generating heat that supports the subsequent diffusive motives.

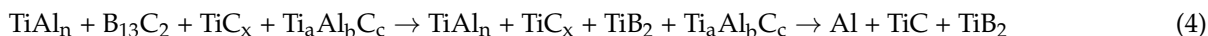
The second step is the diffusion of C in TiAl<sub>n</sub> (Equation (3)).



Carbon atoms diffuse more easily with respect to boron atoms from B<sub>4</sub>C particles [47]. The diffusion of C in TiAl<sub>n</sub> is supported, on one hand, by the increment in temperature guaranteed by the formation of TiAl<sub>n</sub> and, on the other hand, by the counterdiffusion of Al atoms in B<sub>4</sub>C particles, promoting the dissociation of boron carbide. These two phenomena activate the C atoms, which diffuse in TiAl<sub>n</sub> and lead to the development of C-rich zones, promoting the formation of TiC<sub>x</sub>. The synthesis of TiC<sub>x</sub> is strongly exothermic and the heat will help to maintain the TiAl<sub>n</sub> in the melted state and to activate further C atoms inside B<sub>4</sub>C particles. At the same time, depletion in C of B<sub>4</sub>C particles and formation of Ti<sub>a</sub>Al<sub>b</sub>C<sub>c</sub> may occur.

The last step is the diffusion of B in TiAl<sub>n</sub> according to Equation (4), delayed with respect to C diffusion due to its lower diffusivity.





The synthesis of  $\text{TiB}_2$  is similar to that discussed for  $\text{TiC}_x$  and it is caused by the formation of B-rich zones. The precipitation of  $\text{TiC}$  and  $\text{TiB}_2$  grains occurs when the Al-Ti melt reaches a condition of supersaturation.

The synthesis of an in situ A6061/TiC +  $\text{TiB}_2$  composite is beneficial for several reasons:

- TiC and  $\text{TiB}_2$  are commonly used as reinforcements for AMC because of their thermal and chemical stability, and good wettability. The use of these two ceramic phases makes it possible to improve mechanical properties (such as Young's modulus, stiffness, strength, and hardness), and corrosion and wear performances [48,49];
- The A6061 alloy has columnar dendritic solidification and a wide solidification range, which can result in cracking during solidification. The nucleant and grain-refining action of TiC and  $\text{TiB}_2$  for Al alloys [50–52] induces an equiaxed solidification, avoiding crack formation; in fact, both ceramic compounds have a lattice parameter comparable with that of the matrix and they can induce an equiaxed grain growth;
- The in situ synthesis of the grain refiners is beneficial for nucleation sites distribution inside the matrix and the size distribution of these grain refiners [53].

Equation (5) summarizes the reaction mechanism of the A6061 RAM2 system:



According to the manufacturer, the system is designed under the following hypothesis:

- After the LPBF process, the final microstructure would consist of TiC and  $\text{TiB}_2$  particles dispersed in the aluminum matrix;
- The in situ reaction leads to the formation of 2% vol of ceramic reinforcements;
- The system follows the stoichiometry of the reaction; therefore, Ti and  $\text{B}_4\text{C}$  have a molar ratio of 3:1.

Based on these considerations, the theoretical density of the LPBF-ed material and the powder were calculated according to the stoichiometry of the reaction, and they were evaluated to be equal to  $2.7387 \text{ g/cm}^3$  and  $2.7249 \text{ g/cm}^3$ , respectively. A LECO analysis was then performed on the powder to evaluate the content of C inside the powder. Assuming that the measured C content was attributable to the  $\text{B}_4\text{C}$ , it was possible to estimate the density of the powder in accordance with the stoichiometry of the reaction. A value of  $2.7245 \text{ g/cm}^3$  was obtained. The theoretical density and that estimated by the LECO analysis were similar and coherent; both of them were determined based on the hypothesis of a perfectly stoichiometric system and a complete reaction of the powder. The estimated composition of the powder is reported in Table 2.

**Table 2.** Estimated composition of the powder from LECO analysis.

Component	vol.%	wt.%
Al	97.5	96.6
Ti	1.5	2.5
$\text{B}_4\text{C}$	1	0.9

However, the powder density was also measured using a helium pycnometer, and it was evaluated to be  $2.7574 \pm 0.0011 \text{ g/cm}^3$ . Although this value was higher with respect to the previously discussed theoretical and LECO-based densities, it was the only one resulting from a direct measurement of the powder. This pycnometer density value suggests that the composition of the powder is not stoichiometric: it is, in fact, reasonable to suppose that the Ti content was higher than the estimated 1.5% vol. Assuming that the  $\text{B}_4\text{C}$  content was fixed, the density calculated with the pycnometer implied a Ti content of

3.25% vol. Therefore, a higher content of titanium might be justified by the key role of Ti and  $\text{TiAl}_n$  in the reaction mechanism.

### 3.3. Bulk Characterization

In Figure 4, the density values of cubic samples are reported. Because of the lack of information about the composition of the system from the manufacturer (due to the patent) and the not-verified stoichiometric hypothesis, it was not possible to evaluate the effective bulk density and accurately estimate the porosity of the samples.

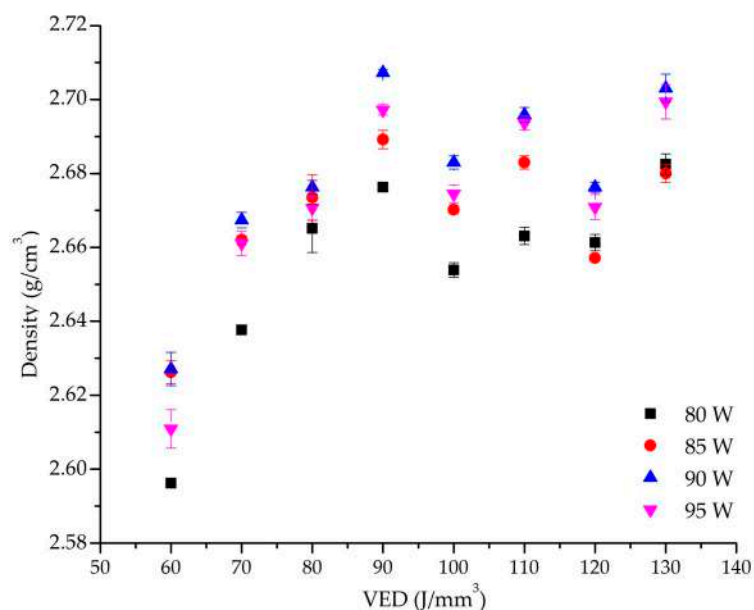


**Figure 4.** Density versus volumetric energy (VED) graph of A6061 RAM2 LPBF-ed samples.

By observing the density trend as a function of laser power, a similar trend can be identified for each tested VED value. In fact, the use of laser power of 80 W leads to lower densities, as expected; indeed, aluminum alloys have high reflectivity and thermal conductivity and require high laser power in order to obtain a complete melting of the alloys [54]. For these reasons, the densities increase using higher laser power: they raise using 85 W and reach their maximum values with 90 W. Finally, the use of 95 W leads to a decrease in densities with respect to those accomplished using 90 W. In fact, laser power that is too high can induce keyhole porosity, gas porosity, and other defects and can lead to lower densities [7,55]. This trend finds validation in the literature: excessively high or low VED values involve lower density and higher porosity [6,7,55,56]. On one hand, low VED might induce partial or no melting of the metal powder; on the other hand, high VED might cause a lack of fusion, evaporation, melt pool instabilities, and gas-induced pores.

The maximum density was achieved using a power laser of 90 W and a VED of 90 J/mm³. This parameter set was used to produce the dogbone specimens and evaluate mechanical properties.

Optical micrographs of the samples obtained by using the optimized set of parameters are shown in Figure 5. It is possible to recognize several unreacted or partially reacted Ti and  $\text{B}_4\text{C}$  particles inside the aluminum matrix (the results of EDS analysis performed on these particles are shown in Figure 6). The presence of these particles suggests that the system does not evolve to the final stage of the reaction mechanism, which would involve the complete consumption of reactants in the matrix and the formation of  $\text{TiC}$  and  $\text{TiB}_2$  particles. Similar considerations have been carried out by Torbati-Sarraf et al. [32] in their study about the corrosion behavior of A6061 RAM2. In their study, the LPBF samples were provided and processed by Elementum 3D using their optimized set of process parameters; despite that, unreacted Ti and  $\text{B}_4\text{C}$  were observed in the microstructures. As a matter of fact, the presence of unreacted particles is one of the major issues in processing in situ

metal matrix composites by LPBF [57]. From Figure 6 it can be observed that, while the  $B_4C$  particles retain their initial morphology and composition after the RAM process, Ti particles exhibit a smaller size and a different shape. It is evident that the Ti particles display two distinct zones, noticeable by the contrast arising from the difference in atomic weight. The inner zone is Ti-rich and corresponds to the unreacted portion of the particle, while the outer zone is a reaction zone consisting of  $TiAl_n$  with variable stoichiometry.

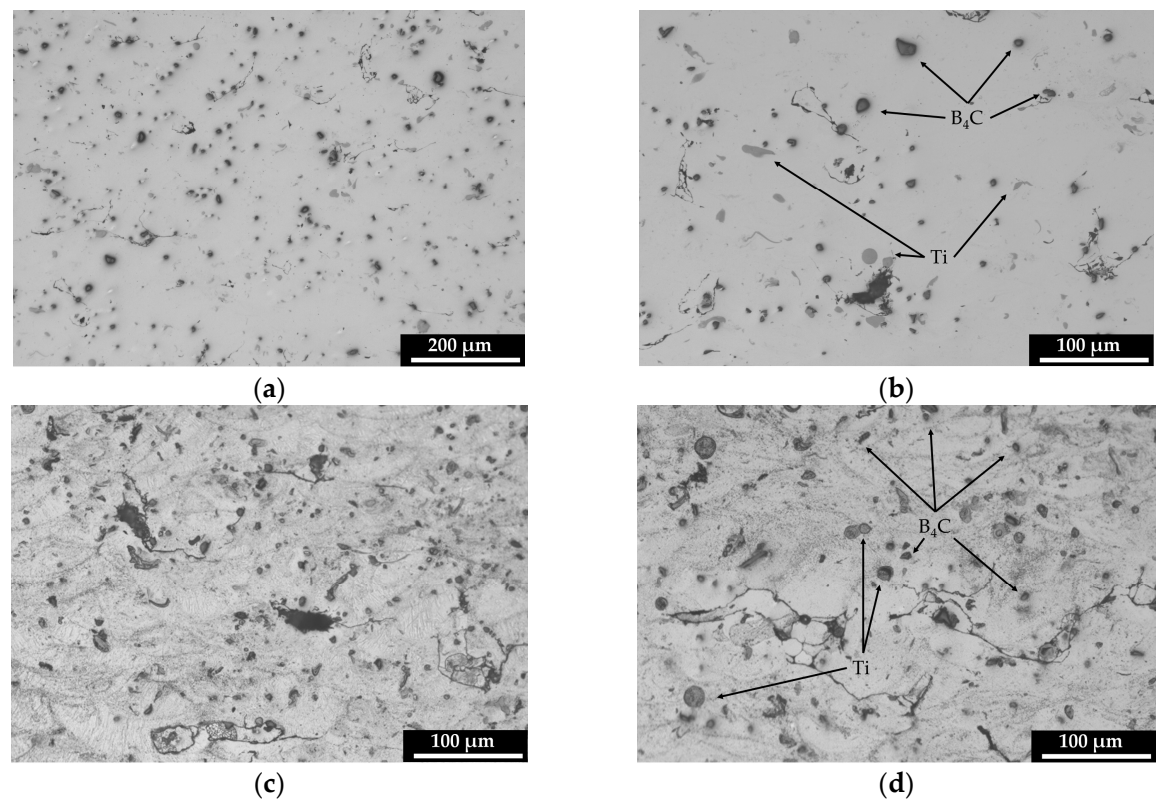


**Figure 5.** Optical micrographs of cubic samples with optimized parameters along z direction at (a) lower and (b–d) higher magnification; (c,d) show microstructure after etching. Micrographs were taken along the building direction.

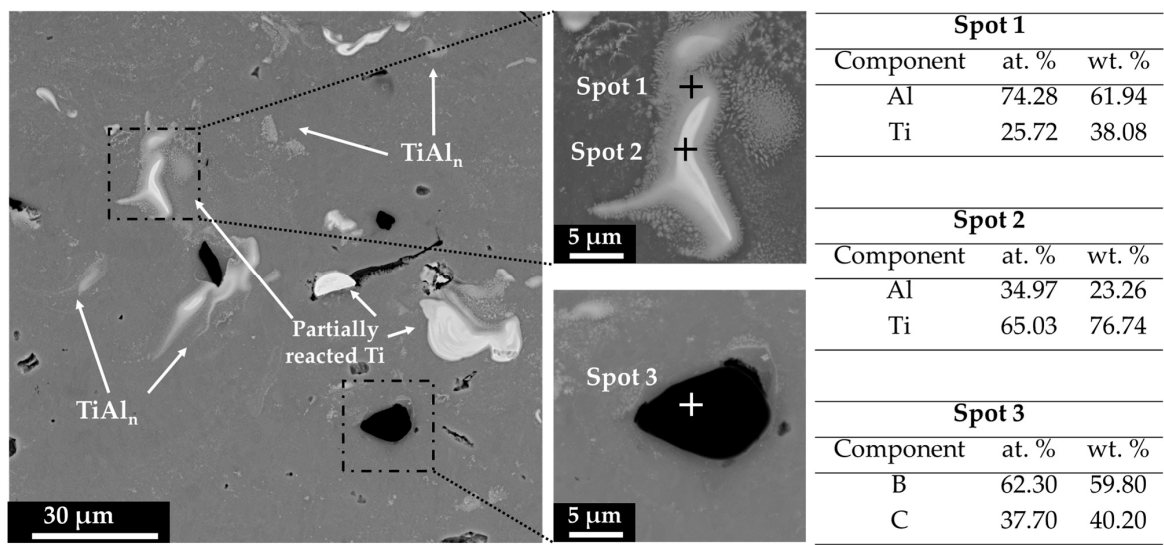


**Figure 6.** High magnification SEM micrographs and EDS analysis of unreacted Ti and  $B_4C$  particles. Micrographs were taken along the building direction (analysis spots are indicated by the “+” sign on micrographs).

At higher magnification (Figure 5b–d), some defects can be observed, such as microcracks, particle detachment (Figure 5b,c), and unmelted particles (Figure 5d).  $B_4C$  particles show debonding at the interface with the Al matrix and microcracks seem propagating from them. The debonding can be explained by the poor wettability of  $B_4C$  particles from melted Al [46,58]. In addition, the thermal mismatch between Al and  $B_4C$  [59], combined with the rapid cooling involved in the LPBF process, can induce interfacial debonding, crack initiation, and propagation [60,61]. A consequence of this debonding is the pull-out of  $B_4C$  particles and the formation of pores that can originate after the polishing procedure, as shown in Figure 5b,c. For this reason, these pores are not attributable to the LPBF process. As a matter of fact, Sullivan et al. [30] characterized crack-free A6061 RAM2 samples processed on an EOS M290 LPBF machine by Elementum 3D (the company owner of the material and the RAM patent, Erie, CO, USA, using a preheating of 200 °C of the building platform. The use of preheating has an important role in avoiding thermal cracks in metal matrix composite, mitigating thermal gradient in the material [61]. Additionally, the preheating might have a beneficial impact on the adhesion between ceramic particles and metal matrix, avoiding particles debonding: in fact, the temperature increment can enhance the wettability of  $B_4C$  particles by molten aluminum and promote a stronger interfacial bond [58,62].

At the same time, neither lack of fusion nor solidification cracking was observed. The morphology of the cracks in the micrographs (Figure 5) is, in fact, different from that of solidification cracks, which are characterized by propagation along the building direction. The absence of this defect, which is characteristic of high-strength aluminum alloys such as A6061, can be justified considering that, although the reaction is not complete, heterogeneous nucleation took place during the solidification.

SEM micrographs of the optimized A6061 RAM2 sample and linear EDS analysis of unreacted Ti and  $B_4C$  particles are reported in Figure 7. It is possible to observe that Ti particles have reacted with melted Al to produce  $TiAl_n$ , as confirmed by the EDS analysis shown in Figure 7a. The stoichiometry of  $TiAl_n$  is not defined: a reaction zone is observable around Ti particles, and linear EDS analyses reveal a concentration gradient of Ti and Al in this zone.  $TiAl_n$  can be located around the unreacted Ti particles and dispersed in the matrix, because of the convective motions during the LPBF process caused by the laser. The presence of  $TiAl_n$  can be justified by the first step of the reaction mechanism (Equation (2)) and confirms that the system has started its in situ reaction.

In addition, EDS analysis conducted on  $B_4C$  particles (Figure 7b) confirmed that the system does not evolve to complete the reaction. As explained earlier, the synthesis of TiC and  $TiB_2$  occurs at the  $TiAl_n/B_4C$  interface, due to the diffusion of B and C in the Ti–Al intermetallic layer. It is conceivable that the Ti content is not sufficient to guarantee the interaction between the intermetallic and carbon boride particles. At the same time, micrographs show several unreacted and partially reacted Ti particles, suggesting that their size may hinder a complete reaction with aluminum to synthesize  $TiAl_n$  and, subsequently, interact with carbon boride particles. Lastly, the use of a powder blend may not ensure optimal dispersion of reactants and uniform reaction in the composite. Therefore, EDS analysis has confirmed the absence of Ti at the interface and reaction zones around  $B_4C$  particles.

In Figure 8, the comparison between the XRD spectrum of the A6061 RAM2 powder and LPBF-ed material is reported. The analysis of the XRD pattern of the bulk material has confirmed the intermediate state of the system, as no evidence of the presence of TiC and  $TiB_2$  has been detected. Quite the opposite, the presence of the intermediate  $TiAl_3$  and  $TiAl_2$  (observed in the micrographs) has been confirmed by the XRD analysis, as shown in Figure 8b.



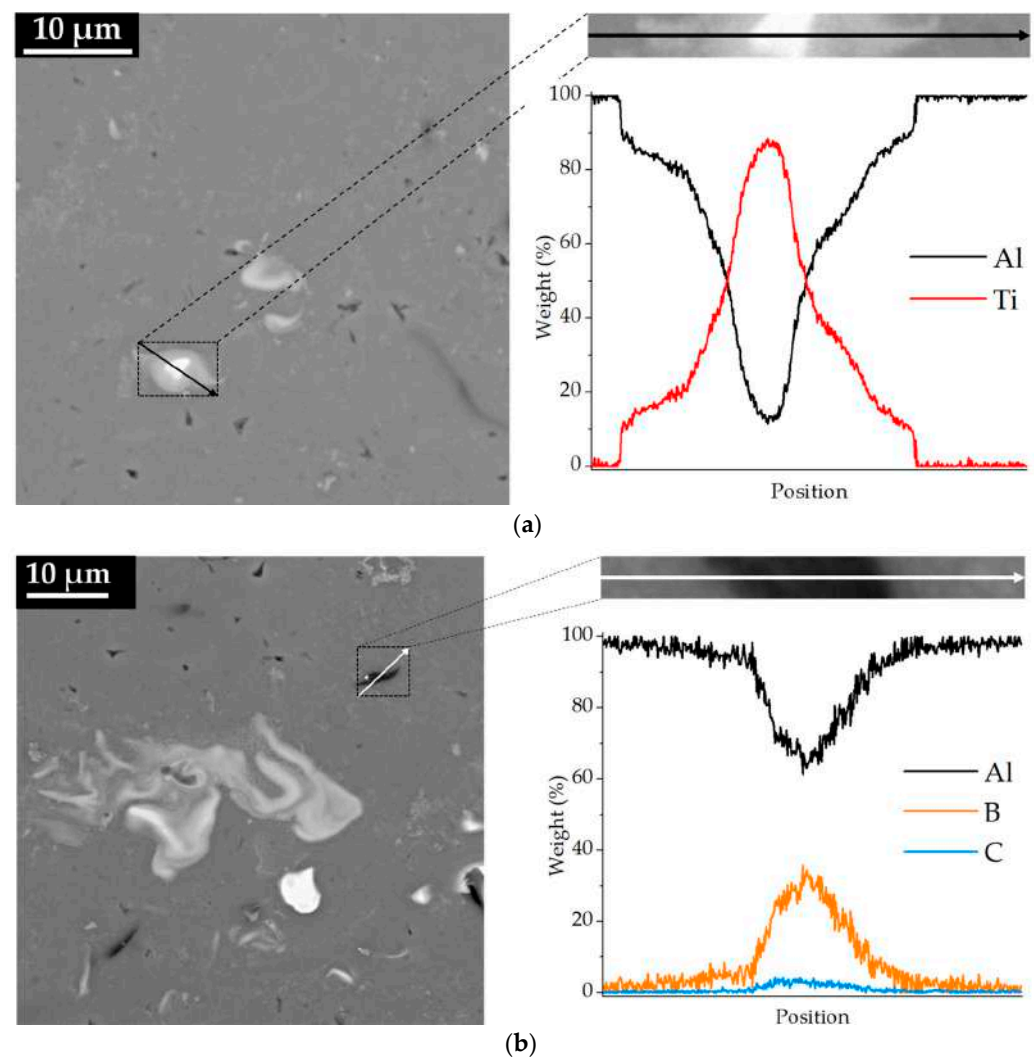


**Figure 7.** High magnification SEM micrographs of optimized cubic sample and linear EDS analysis of (a) Ti and (b) B<sub>4</sub>C particles.

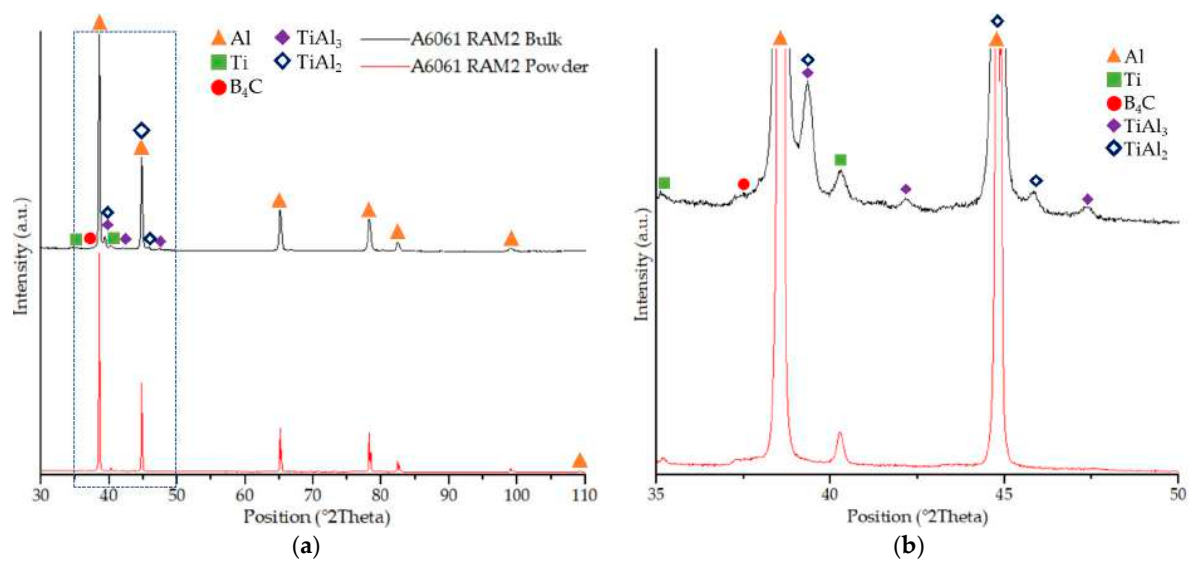


**Figure 8.** (a) XRD patterns of A6061 RAM2 powder and bulk samples. (b) Magnification at low intensities in the range of 35–50°.

Tensile properties of as-built dog-bone A6061 RAM2 specimens (printed using the optimized process parameters set) have been reported in Table 3 and compared with tensile properties of as-built LPBF-ed A6061 processed with similar process parameters (Concept Laser MLab R, P = 95 W, VED = 93 J/mm<sup>3</sup>) [35] and A6061 RAM2 processed by Elementum 3D [30]. In their study, Bradford et al. produced pure A6061 for LPBF using process parameters similar to those used in this study, and they observed severe solidification cracking in the produced samples. Micrographs of LPBF-ed pure A6061 showed severe solidification cracking characterized by cracks propagated along the building direction. The evaluation of tensile properties confirmed the deleterious impact of solidification cracks on the mechanical properties of the LPBF-ed material.

**Table 3.** Tensile properties of A6061 RAM2 and as-built LPBF-ed A6061 [35].

Properties	A6061 RAM2	E3D A6061 RAM2 [30]	A6061 [35]
E (GPa)	73 ± 6	74	27.6
$\sigma_y$ (MPa)	230 ± 6	-	56.6
UTS (MPa)	256 ± 11	234.3	62.1
$\epsilon_r$ (%)	4 ± 1.6	-	0.7

In addition, Sullivan et al. [30] characterized two different formulations of A6061 RAM (with 2 and 10 vol.% of inoculants) processed by LPBF and electron beam freeform fabrication (EB-FF). In their study, A6061 RAM2 samples were provided by Elementum 3D and processed by LPBF (EOS M290) using the optimized parameters set suggested by the company. For the same formulation (A6061 RAM2), the UTS was reported as 234.3 MPa, while Young's modulus was evaluated as 74 GPa. Despite the use of the same powder and optimized process parameters, these results are lower than those obtained in this study by processing A6061 RAM2 with a low-power LPBF machine.

In the case of A6061 RAM2 processed in this study, tensile properties are superior to those experienced for pure A6061 [35]. Given the use of similar process parameters, two significant differences can be identified in A6061 RAM2. First, the presence of Ti and B<sub>4</sub>C in the system increases the absorptivity of the powder [42,63,64]; therefore, the energy transferred to the powder bed is higher with the same parameters and VED.

Second, notwithstanding the incomplete reaction of the system and the absence of TiC and TiB<sub>2</sub> in the final microstructure, no solidification cracking was observed in the processed material. The equiaxed solidification should be provided by the in situ synthesis of the final ceramic phases, but experimental characterization has confirmed that the system does not evolve to the final stage. Because of the absence of the designed grain refiners and the lack of solidification cracking, it is possible to hypothesize that another phase allows for equiaxed solidification. It is reasonable to assume that TiAl<sub>n</sub> might have had a key role in hindering columnar grain growth and inducing the formation of equiaxed grains. Especially TiAl<sub>3</sub> has a small lattice mismatch with respect to Al and it has been experienced as an effective nucleant for Al alloys [65,66]. It can be concluded that equiaxed solidification occurs, even though the system does not evolve to the final microstructure and the synthesis of TiC and TiB<sub>2</sub> does not take place, due to the in situ formation of TiAl<sub>3</sub>, which acts as an efficient nucleant for A6061 alloy.

As explained previously, the expected microstructure of LPBF-processed A6061 (and other high-strength aluminum alloys) consists of large columnar grains grown along the building direction [28,67,68]. These grains develop through several melt pool layers due to remelting of the previous layer and subsequent epitaxial growth. In addition, their morphology does not allow them to accommodate the strains caused by shrinkage during solidification, resulting in solidification cracking.

SEM micrographs of the etched cross-section are reported in Figure 9. Chemical etching enables the visualization of melt pools and a bimodal microstructure: in fact, it can be observed the presence of fine equiaxed grains (with dimensions between 1 and 5 µm) at melt pool boundaries, and columnar grains in the inner part of the melt pool (perpendicular



to the melt pool boundaries). The presence of both equiaxial and columnar fine grains in the LPBF-processed A6061 RAM2 indicates a change in the solidification mechanism compared to the unmodified A6061 alloy processed by LPBF. It is worth noting that Mehta et al. [28] obtained a similar microstructure in Zr-modified A6061 fabricated by LPBF. In their study, the authors compared the microstructure of as-built A6061 and Zr-modified A6061, explaining the role of  $\text{Al}_3\text{Zr}$  as a nucleant, especially at the bottom of the melt pools. In fact, A6061 aluminum alloy processed by LPBF experienced severe columnar grain growth across the melt pools and a consequent solidification cracking. The addition of inoculants in the system made it possible to induce heterogeneous nucleation and obtain a refined microstructure. Furthermore, they observed the presence of fine equiaxed grains at melt pool boundaries because of the slower solidification front velocity and the lower temperature (with respect to the center of the melt pool), optimally sized nucleant particles are more stable and capable to induce heterogeneous nucleation. Similarly, Xi et al. [69] investigated the effect induced by the addition of nano- $\text{TiB}_2$  particles on the microstructure of LPBF-ed  $\text{AlSi10Mg}$ . The authors observed a strong correlation between the addition of inoculant particles and the refinement grade: as the  $\text{TiB}_2$  content grew, the portion of refined microstructure increased because the number of nucleation sites raised. Adding 1–2% weight of  $\text{TiB}_2$  resulted in partial refinement of the microstructure and the presence of equiaxial zones at the melt pool boundaries. Further increasing the  $\text{TiB}_2$  content extended the refinement to the inside of the melt pool.

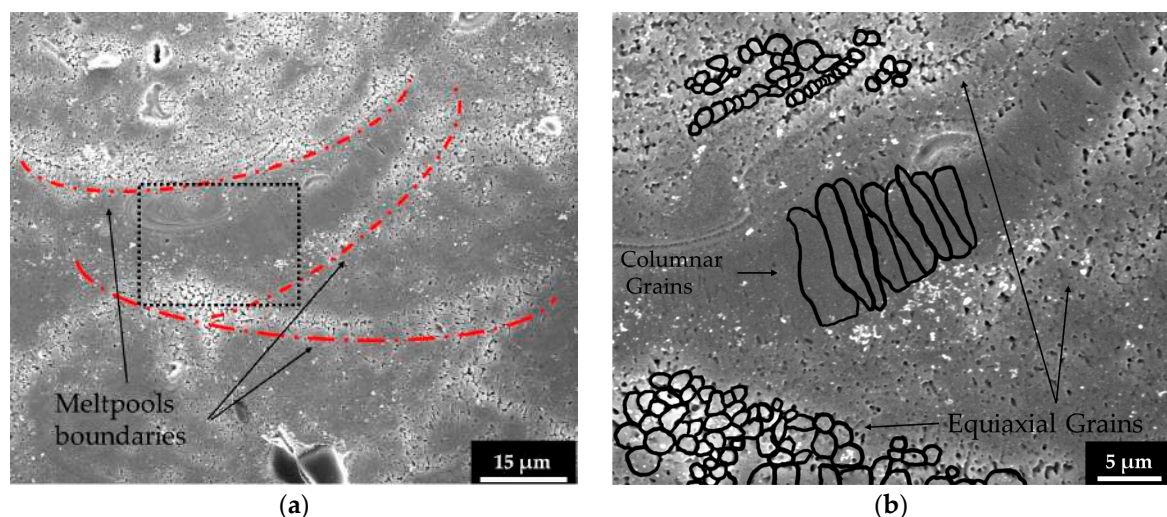


**Figure 9.** SEM micrographs of the etched cross-section (micrographs were taken in SED). (a) Low magnification micrograph. (b) High magnification of the underlined area in (a).

Therefore, the partial refinement that has occurred in LPBF-processed A6061 RAM2 can be explained by two factors: (i) the higher stability at the melt pool boundaries and (ii) the number of optimally sized  $\text{TiAl}_n$  particles [70,71]. Metallographic observation of the processed material (Figures 5, 6, and 7a) underlined the presence of unreacted and partially reacted Ti particles, and not dispersed  $\text{TiAl}_n$  within the matrix. It is reasonable to assume that the micrometric size of Ti particles may hinder the synthesis of a sufficient number of optimally sized  $\text{TiAl}_n$  particles. At the same time, this might occur at the melt pool boundaries because of the remelting of the previous layer. The equiaxial grains at the bottom of the melt pool can interrupt the epitaxial growth of columnar grains, which are confined within the melt pool and have smaller sizes with respect to LPBF-ed high-strength aluminum alloys.

Furthermore, although the presence of equiaxial grains is localized only at the melt pool boundaries, they can improve the resistance of the material to solidification cracking. On one hand, fine equiaxial grains can accommodate shrinkage-generated strains more easily than columnar grains. On the other hand, they can hinder the propagation of

intergranular cracks that are triggered within the melt pool and propagate along the building direction and across the melt pools [28].

#### 4. Conclusions

In this work, the effect of in situ synthesized grain refiners on the processability for LPBF of A6061 aluminum alloy has been investigated. The commercial A6061 RAM2 powder was extensively examined to understand its composition and its evolution during the LPBF process. Process parameters optimization was conducted to assess their influence on the density and processability of the alloy. Finally, the mechanical characterization of the material processed using the optimized parameters set has been performed. The main conclusions are reported in the following:

1. A6061 RAM2 is a suitable material for the LPBF process, designed to obtain an aluminum matrix composite reinforced with ceramic phases through the reactive LPBF process. The powder consists of three components—Al, Ti, and  $B_4C$  particles—which are capable of reacting with each other to synthesize TiC and  $TiB_2$ . These synthesized phases are expected to act as nucleants for the A6061 alloy.
2. The process parameters optimization performed on the material showed that the highest density can be achieved using a laser power of 90 W and a scanning speed of 635 mm/s, resulting in a VED of  $90 \text{ J/mm}^3$ . Specifically, for all tested VED values, a power of 90 W ensures higher densities.
3. The LPBF process initiates the reaction mechanism, but this does not evolve into a complete reaction. Evidence of the presence of  $TiAl_2$  and  $TiAl_3$  was found in the processed material, in agreement with the reaction mechanism. However, TiC and  $TiB_2$  were not detected in the final microstructure.
4. Despite the absence of TiC and  $TiB_2$ , which are expected to act as grain refiners for the A6061 matrix, solidification cracking does not affect the processed material. This absence suggests that  $TiAl_3$  may act as a heterogeneous nucleation site and induces an equiaxial solidification of the matrix:  $TiAl_3$  is known as an effective nucleant for aluminum alloys, as confirmed in the literature. Chemical etching revealed partial refinement and a bimodal microstructure, consisting of fine equiaxial grain at the melt pool boundaries which can inhibit solidification cracks. At the same time, further investigation is required to understand the role of titanium particle size and process parameters in the synthesis of  $TiAl_3$  particles and their function as nucleants.
5. Defects such as pores and microcracks can be observed in the microstructure. These defects are attributed to the interaction between the Al matrix and  $B_4C$  particles, resulting from thermal mismatch and weak interfacial bonding. Further investigation is, however, needed to mitigate these phenomena, including exploring the role of preheating.
6. Despite the presence of defects in the LPBF-ed material, the mechanical properties of the optimized process material are considerably superior to those obtained by processing pure A6061 using LPBF. A6061 RAM2, with Young's modulus of  $73 \pm 6 \text{ GPa}$  and a yield stress of  $230 \pm 6 \text{ MPa}$ , exhibits significantly higher values compared to the pure A6061 alloy processed for LPBF, which has Young's modulus of  $27.6 \text{ GPa}$  and a yield stress of  $56.6 \text{ MPa}$ , respectively.

**Author Contributions:** Conceptualization, E.P., F.G., R.S., F.B. and C.F.B.; methodology, M.R., E.P., F.G., F.B. and C.F.B.; validation, M.R., M.V. and E.P.; investigation, M.R. and M.V.; data curation M.R., M.V. and E.P.; writing—original draft preparation, M.R.; writing—review and editing, M.R., E.P., F.B. and C.F.B.; visualization, M.R.; supervision, E.P., F.G., R.S., F.B. and C.F.B. All authors have read and agreed to the published version of the manuscript.

**Funding:** This research received no external funding.

**Data Availability Statement:** The data presented in this study are available on request from the corresponding author.

**Acknowledgments:** The authors would like to acknowledge Serena Lerda of Politecnico di Torino for conducting the SEM analysis.

**Conflicts of Interest:** The authors declare no conflict of interest.

## References

1. Khorasani, M.; Gibson, I.; Ghasemi, A.H.; Hadavi, E.; Rolfe, B. Laser Subtractive and Laser Powder Bed Fusion of Metals: Review of Process and Production Features. *Rapid Prototyp. J.* **2023**, *29*, 935–958. [\[CrossRef\]](#)
2. Aversa, A.; Marchese, G.; Saboori, A.; Bassini, E.; Manfredi, D.; Biamino, S.; Ugues, D.; Fino, P.; Lombardi, M. New Aluminum Alloys Specifically Designed for Laser Powder Bed Fusion: A Review. *Materials* **2019**, *12*, 1007. [\[CrossRef\]](#) [\[PubMed\]](#)
3. Sing, S.L.; Yeong, W.Y. Laser Powder Bed Fusion for Metal Additive Manufacturing: Perspectives on Recent Developments. *Virtual Phys. Prototyp.* **2020**, *15*, 359–370. [\[CrossRef\]](#)
4. Khorasani, A.M.; Gibson, I.; Veetil, J.K.; Ghasemi, A.H. A Review of Technological Improvements in Laser-Based Powder Bed Fusion of Metal Printers. *Int. J. Adv. Manuf. Technol.* **2020**, *108*, 191–209. [\[CrossRef\]](#)
5. Campbell, I.; Bourell, D.; Gibson, I. Additive Manufacturing: Rapid Prototyping Comes of Age. *Rapid Prototyp. J.* **2012**, *18*, 255–258. [\[CrossRef\]](#)
6. Aboulkhair, N.T.; Simonelli, M.; Parry, L.; Ashcroft, I.; Tuck, C.; Hague, R. 3D Printing of Aluminium Alloys: Additive Manufacturing of Aluminium Alloys Using Selective Laser Melting. *Prog. Mater. Sci.* **2019**, *106*, 100578. [\[CrossRef\]](#)
7. Galy, C.; Le Guen, E.; Lacoste, E.; Arvieu, C. Main Defects Observed in Aluminum Alloy Parts Produced by SLM: From Causes to Consequences. *Addit. Manuf.* **2018**, *22*, 165–175. [\[CrossRef\]](#)
8. Padovano, E.; Badini, C.; Pantarelli, A.; Gili, F.; D’Aiuto, F. A Comparative Study of the Effects of Thermal Treatments on AlSi10Mg Produced by Laser Powder Bed Fusion. *J. Alloys Compd.* **2020**, *831*, 154822. [\[CrossRef\]](#)
9. Aboulkhair, N.T.; Maskery, I.; Tuck, C.; Ashcroft, I.; Everitt, N.M. The Microstructure and Mechanical Properties of Selectively Laser Melted AlSi10Mg: The Effect of a Conventional T6-like Heat Treatment. *Mater. Sci. Eng. A* **2016**, *667*, 139–146. [\[CrossRef\]](#)
10. Wu, J.; Wang, X.Q.; Wang, W.; Attallah, M.M.; Loretto, M.H. Microstructure and Strength of Selectively Laser Melted AlSi10Mg. *Acta Mater.* **2016**, *117*, 311–320. [\[CrossRef\]](#)
11. Hyer, H.; Zhou, L.; Park, S.; Gottsfritz, G.; Benson, G.; Tolentino, B.; McWilliams, B.; Cho, K.; Sohn, Y. Understanding the Laser Powder Bed Fusion of AlSi10Mg Alloy. *Metallogr. Microstruct. Anal.* **2020**, *9*, 484–502. [\[CrossRef\]](#)
12. Azizi, A.; Hejripour, F.; Goodman, J.A.; Kulkarni, P.A.; Chen, X.; Zhou, G.; Schiffres, S.N. Process-Dependent Anisotropic Thermal Conductivity of Laser Powder Bed Fusion AlSi10Mg: Impact of Microstructure and Aluminum-Silicon Interfaces. *Rapid Prototyp. J.* **2023**, *29*, 1109–1120. [\[CrossRef\]](#)
13. Aboulkhair, N.T.; Everitt, N.M.; Ashcroft, I.; Tuck, C. Reducing Porosity in AlSi10Mg Parts Processed by Selective Laser Melting. *Addit. Manuf.* **2014**, *1*, 77–86. [\[CrossRef\]](#)
14. Kimura, M.; Hirayama, A.; Yoshioka, J.; Maekawa, H.; Kusaka, M.; Kaizu, K.; Takahashi, T. Mechanical Properties of AlSi12 Alloy Manufactured by Laser Powder Bed Fusion Technique. *J. Fail. Anal. Prev.* **2020**, *20*, 1884–1895. [\[CrossRef\]](#)
15. Ghasemi, A.; Fereiduni, E.; Balbaa, M.; Elbestawi, M.; Habibi, S. Unraveling the Low Thermal Conductivity of the LPBF Fabricated Pure Al, AlSi12, and AlSi10Mg Alloys through Substrate Preheating. *Addit. Manuf.* **2022**, *59*, 103148. [\[CrossRef\]](#)
16. Vanzetti, M.; Virgillito, E.; Aversa, A.; Manfredi, D.; Bondioli, F.; Lombardi, M.; Fino, P. Short Heat Treatments for the F357 Aluminum Alloy Processed by Laser Powder Bed Fusion. *Materials* **2021**, *14*, 6157. [\[CrossRef\]](#)
17. Lorenzetti, L.; Tonelli, L.; Ceschini, L.; Liverani, E.; Martini, C. A357 Aluminium Alloy Produced by LPBF: Tribological Behaviour in Dry Sliding Conditions. *Wear* **2022**, *510–511*, 204488. [\[CrossRef\]](#)
18. Cheng, C.C.; Li, Z.; Dhillon, J.S.; Hudon, P.; Brochu, M. Influence of Powder Layer Thickness on Microstructure and T5 Heat Treatability of F357 Alloy Fabricated by Laser Powder Bed Fusion Process. *J. Alloys Compd.* **2023**, *948*, 169633. [\[CrossRef\]](#)
19. Aversa, A.; Marchese, G.; Manfredi, D.; Lorusso, M.; Calignano, F.; Biamino, S.; Lombardi, M.; Fino, P.; Pavese, M. Laser Powder Bed Fusion of a High Strength Al-Si-Zn-Mg-Cu Alloy. *Metals* **2018**, *8*, 300. [\[CrossRef\]](#)
20. Rometsch, P.A.; Zhu, Y.; Wu, X.; Huang, A. Review of High-Strength Aluminium Alloys for Additive Manufacturing by Laser Powder Bed Fusion. *Mater. Des.* **2022**, *219*, 110779. [\[CrossRef\]](#)
21. Zhang, X.; Zheng, H.; Yu, W. A Review on Solidification Cracks in High-Strength Aluminum Alloys via Laser Powder Bed Fusion. *Mater. Today Proc.* **2022**, *70*, 465–469. [\[CrossRef\]](#)
22. Martin, J.H.; Yahata, B.D.; Hundley, J.M.; Mayer, J.A.; Schaedler, T.A.; Pollock, T.M. 3D Printing of High-Strength Aluminium Alloys. *Nature* **2017**, *549*, 365–369. [\[CrossRef\]](#) [\[PubMed\]](#)
23. Maamoun, A.H.; Xue, Y.F.; Elbestawi, M.A.; Veldhuis, S.C. The Effect of Selective Laser Melting Process Parameters on the Microstructure and Mechanical Properties of Al6061 and AlSi10Mg Alloys. *Materials* **2018**, *12*, 12. [\[CrossRef\]](#) [\[PubMed\]](#)
24. Li, G.; Li, X.; Guo, C.; Zhou, Y.; Tan, Q.; Qu, W.; Li, X.; Hu, X.; Zhang, M.X.; Zhu, Q. Investigation into the Effect of Energy Density on Densification, Surface Roughness and Loss of Alloying Elements of 7075 Aluminium Alloy Processed by Laser Powder Bed Fusion. *Opt. Laser Technol.* **2022**, *147*, 107621. [\[CrossRef\]](#)
25. Hyer, H.; Zhou, L.; Mehta, A.; Park, S.; Huynh, T.; Song, S.; Bai, Y.; Cho, K.; McWilliams, B.; Sohn, Y. Composition-Dependent Solidification Cracking of Aluminum-Silicon Alloys during Laser Powder Bed Fusion. *Acta Mater.* **2021**, *208*, 116698. [\[CrossRef\]](#)



26. Montero Sistiaga, M.L.; Mertens, R.; Vrancken, B.; Wang, X.; van Hooreweder, B.; Kruth, J.P.; van Humbeeck, J. Changing the Alloy Composition of Al7075 for Better Processability by Selective Laser Melting. *J. Mater. Process Technol.* **2016**, *238*, 437–445. [\[CrossRef\]](#)
27. Uddin, S.Z.; Murr, L.E.; Terrazas, C.A.; Morton, P.; Roberson, D.A.; Wicker, R.B. Processing and Characterization of Crack-Free Aluminum 6061 Using High-Temperature Heating in Laser Powder Bed Fusion Additive Manufacturing. *Addit. Manuf.* **2018**, *22*, 405–415. [\[CrossRef\]](#)
28. Mehta, A.; Zhou, L.; Huynh, T.; Park, S.; Hyer, H.; Song, S.; Bai, Y.; Imholte, D.D.; Woolstenhulme, N.E.; Wachs, D.M.; et al. Additive Manufacturing and Mechanical Properties of the Dense and Crack Free Zr-Modified Aluminum Alloy 6061 Fabricated by the Laser-Powder Bed Fusion. *Addit. Manuf.* **2021**, *41*, 101966. [\[CrossRef\]](#)
29. Nuechterlein, J.S.; Iten, J.J. Reactive Additive Manufacturing. U.S. Patent US20160271878A1, 17 December 2019. pp. 1–20.
30. Sullivan, E.; Polizzi, A.; Iten, J.; Nuechterlein, J.; Domack, M.; Liu, S. Microstructural Characterization and Tensile Behavior of Reaction Synthesis Aluminum 6061 Metal Matrix Composites Produced via Laser Beam Powder Bed Fusion and Electron Beam Freeform Fabrication. *Int. J. Adv. Manuf. Technol.* **2022**, *121*, 2197–2218. [\[CrossRef\]](#)
31. Waller, D.; Polizzi, A.J.; Iten, J.J. Feasibility Study of Additively Manufactured Al-6061 Ram2 Parts for Aerospace Applications. In Proceedings of the AIAA Scitech 2019 Forum, San Diego, CA, USA, 7–11 January 2019; American Institute of Aeronautics and Astronautics Inc. (AIAA): Reston, VA, USA, 2019.
32. Torbati-Sarraf, H.; Torbati-Sarraf, S.A.; Chawla, N.; Poursaei, A. A Comparative Study of Corrosion Behavior of an Additively Manufactured Al-6061 RAM2 with Extruded Al-6061 T6. *Corros. Sci.* **2020**, *174*, 108838. [\[CrossRef\]](#)
33. Weingarten, C.; Buchbinder, D.; Pirch, N.; Meiners, W.; Wissenbach, K.; Poprawe, R. Formation and Reduction of Hydrogen Porosity during Selective Laser Melting of AlSi10Mg. *J. Mater. Process Technol.* **2015**, *221*, 112–120. [\[CrossRef\]](#)
34. Tan, J.H.; Wong, W.L.E.; Dalgarno, K.W. An Overview of Powder Granulometry on Feedstock and Part Performance in the Selective Laser Melting Process. *Addit. Manuf.* **2017**, *18*, 228–255. [\[CrossRef\]](#)
35. Bradford, R.L.; Cao, L.; Klosterman, D.; Herman, F.; Forman, L.; Browning, C. A Metal–Metal Powder Formulation Approach for Laser Additive Manufacturing of Difficult-to-Print High-Strength Aluminum Alloys. *Mater. Lett.* **2021**, *300*, 130113. [\[CrossRef\]](#)
36. Jandaghi, M.R.; Pouraliakbar, H.; Fallah, V.; Ghassemali, E.; Saboori, A.; Pavese, M. Additive Manufacturing of Nano-Oxide Decorated AlSi10Mg Composites: A Comparative Study on Gd<sub>2</sub>O<sub>3</sub> and Er<sub>2</sub>O<sub>3</sub> Additions. *Mater. Charact.* **2022**, *192*, 112206. [\[CrossRef\]](#)
37. Martucci, A.; Aversa, A.; Manfredi, D.; Bondioli, F.; Biamino, S.; Ugues, D.; Lombardi, M.; Fino, P. Low-Power Laser Powder Bed Fusion Processing of Scalmalloy®. *Materials* **2022**, *15*, 3123. [\[CrossRef\]](#) [\[PubMed\]](#)
38. ASTM International. *Designation: E8/E8M—22 Standard Test Methods for Tension Testing of Metallic Materials 1*; ASTM International: West Conshohocken, PA, USA, 2022.
39. British Standards Institution. *Metallic Materials: Tensile Testing. Part 1, Method of Test at Room Temperature*; CEN-CENELEC Management Centre: Brussels, Belgium, 2020; ISBN 9780539047356.
40. Riener, K.; Albrecht, N.; Ziegelmeier, S.; Ramakrishnan, R.; Haferkamp, L.; Spierings, A.B.; Leichtfried, G.J. Influence of Particle Size Distribution and Morphology on the Properties of the Powder Feedstock as Well as of AlSi10Mg Parts Produced by Laser Powder Bed Fusion (LPBF). *Addit. Manuf.* **2020**, *34*, 101286. [\[CrossRef\]](#)
41. Chang, F.; Gu, D.; Dai, D.; Yuan, P. Selective Laser Melting of In-Situ Al<sub>4</sub>SiC<sub>4</sub> + SiC Hybrid Reinforced Al Matrix Composites: Influence of Starting SiC Particle Size. *Surf. Coat. Technol.* **2015**, *272*, 15–24. [\[CrossRef\]](#)
42. Gu, D.; Yang, Y.; Xi, L.; Yang, J.; Xia, M. Laser Absorption Behavior of Randomly Packed Powder-Bed during Selective Laser Melting of SiC and TiB<sub>2</sub> Reinforced Al Matrix Composites. *Opt. Laser. Technol.* **2019**, *119*, 105600. [\[CrossRef\]](#)
43. Ro, C.U.; Osán, J.; Van Grieken, R. Determination of Low-Z Elements in Individual Environmental Particles Using Windowless EPMA. *Anal. Chem.* **1999**, *71*, 1521–1528. [\[CrossRef\]](#)
44. Elementum 3D. *A6061-RAM2 (Highly Versatile and Cost Effective)*; Elementum 3D: Erie, CO, USA, 2021.
45. Dadbakhsh, S.; Mertens, R.; Hao, L.; Van Humbeeck, J.; Kruth, J.P. Selective Laser Melting to Manufacture “In Situ” Metal Matrix Composites: A Review. *Adv. Eng. Mater.* **2019**, *21*, 1801244. [\[CrossRef\]](#)
46. Shen, P.; Zou, B.; Jin, S.; Jiang, Q. Reaction Mechanism in Self-Propagating High Temperature Synthesis of TiC-TiB<sub>2</sub>/Al Composites from an Al-Ti-B<sub>4</sub>C System. *Mater. Sci. Eng. A* **2007**, *454–455*, 300–309. [\[CrossRef\]](#)
47. Brodtkin, D.; Kalidindi Surya, R.; Barsoum Michel, W.; Zavaliangos, A. Microstructural Evolution during Transient Plastic Phase Processing of Titanium Carbide-Titanium Boride Composites. *J. Am. Ceram. Soc.* **1996**, *79*, 1945–1952. [\[CrossRef\]](#)
48. Minasyan, T.; Hussainova, I. Laser Powder-Bed Fusion of Ceramic Particulate Reinforced Aluminum Alloys: A Review. *Materials* **2022**, *15*, 2467. [\[CrossRef\]](#) [\[PubMed\]](#)
49. Karabulut, Y.; Ünal, R. Additive Manufacturing of Ceramic Particle-Reinforced Aluminum-based Metal Matrix Composites: A Review. *J. Mater. Sci.* **2022**, *57*, 19212–19242. [\[CrossRef\]](#)
50. Mertens, A.I.; Lecomte-Beckers, J. On the Role of Interfacial Reactions, Dissolution and Secondary Precipitation during the Laser Additive Manufacturing of Metal Matrix Composites: A Review. In *New Trends in 3D Printing*; InTech: Vienna, Austria, 2016.
51. Aversa, A.; Marchese, G.; Lorusso, M.; Calignano, F.; Biamino, S.; Ambrosio, E.P.; Manfredi, D.; Fino, P.; Lombardi, M.; Pavese, M. Microstructural and Mechanical Characterization of Aluminum Matrix Composites Produced by Laser Powder Bed Fusion. *Adv. Eng. Mater.* **2017**, *19*, 1700180. [\[CrossRef\]](#)

52. Yi, J.; Zhang, X.; Rao, J.H.; Xiao, J.; Jiang, Y. In-Situ Chemical Reaction Mechanism and Non-Equilibrium Microstructural Evolution of (TiB<sub>2</sub> + TiC)/AlSi10Mg Composites Prepared by SLM-CS Processing. *J. Alloys Compd.* **2021**, *857*, 157553. [\[CrossRef\]](#)
53. Jiang, H.; Song, Y.; Zhang, L.; He, J.; Li, S.; Zhao, J. Efficient Grain Refinement of Al Alloys Induced by In-Situ Nanoparticles. *J. Mater. Sci. Technol.* **2022**, *124*, 14–25. [\[CrossRef\]](#)
54. Buchbinder, D.; Meiners, W.; Pirch, N.; Wissenbach, K.; Schrage, J. Investigation on Reducing Distortion by Preheating during Manufacture of Aluminum Components Using Selective Laser Melting. *J. Laser Appl.* **2014**, *26*, 012004. [\[CrossRef\]](#)
55. Kimura, T.; Nakamoto, T. Microstructures and Mechanical Properties of A356 (AlSi7Mg0.3) Aluminum Alloy Fabricated by Selective Laser Melting. *Mater. Des.* **2016**, *89*, 1294–1301. [\[CrossRef\]](#)
56. Olakanmi, E.O.; Cochrane, R.F.; Dalgarno, K.W. A Review on Selective Laser Sintering/Melting (SLS/SLM) of Aluminium Alloy Powders: Processing, Microstructure, and Properties. *Prog. Mater. Sci.* **2015**, *74*, 401–477. [\[CrossRef\]](#)
57. Dadkhah, M.; Mosallanejad, M.H.; Iuliano, L.; Saboori, A. A Comprehensive Overview on the Latest Progress in the Additive Manufacturing of Metal Matrix Composites: Potential, Challenges, and Feasible Solutions. *Acta Metall. Sin.* **2021**, *34*, 1173–1200. [\[CrossRef\]](#)
58. Malaki, M.; Tehrani, A.F.; Niroumand, B.; Gupta, M. Wettability in Metal Matrix Composites. *Metals* **2021**, *11*, 1034. [\[CrossRef\]](#)
59. Kimmari, E.; Kommel, L. Thermally Induced Cracking in Aluminum/Boron Carbide Composite. In Proceedings of the Proceedings of the International Conference of DAAAM Baltic “Industrial Engineering”, Tallinn, Estonia, 24–26 April 2008; Kyttner, R., Ed.; DAAAM International: Tallinn, Estonia, 2008.
60. Dash, K.; Sukumaran, S.; Ray, B.C. The Behaviour of Aluminium Matrix Composites under Thermal Stresses. *Sci. Eng. Compos. Mater.* **2016**, *23*, 1–20. [\[CrossRef\]](#)
61. Essien, U.; Vaudreuil, S. Issues in Metal Matrix Composites Fabricated by Laser Powder Bed Fusion Technique: A Review. *Adv. Eng. Mater.* **2022**, *24*, 2200055. [\[CrossRef\]](#)
62. Hashim, J.; Looney, L.; Hashmi, M. The Wettability of SiC Particles by Molten Aluminium Alloy. *J. Mater. Process Technol.* **2001**, *119*, 324–328. [\[CrossRef\]](#)
63. Dai, D.; Gu, D.; Xia, M.; Ma, C.; Chen, H.; Zhao, T.; Hong, C.; Gasser, A.; Poprawe, R. Melt Spreading Behavior, Microstructure Evolution and Wear Resistance of Selective Laser Melting Additive Manufactured AlN/AlSi10Mg Nanocomposite. *Surf. Coat. Technol.* **2018**, *349*, 279–288. [\[CrossRef\]](#)
64. Müller, S.; Woizeschke, P. Feasibility of a Laser Powder Bed Fusion Process for Additive Manufacturing of Hybrid Structures Using Aluminum-Titanium Powder-Substrate Pairings. *Addit. Manuf.* **2021**, *48*, 102377. [\[CrossRef\]](#)
65. Liu, X.; Liu, Y.; Zhou, Z.; Wang, K.; Zhan, Q.; Xiao, X. Grain Refinement and Crack Inhibition of Selective Laser Melted AA2024 Aluminum Alloy via Inoculation with TiC–TiH<sub>2</sub>. *Mater. Sci. Eng. A* **2021**, *813*, 141171. [\[CrossRef\]](#)
66. Fan, Z.; Yan, X.; Fu, Z.; Niu, B.; Chen, J.; Hu, Y.; Chang, C.; Yi, J. In Situ Formation of D0<sub>22</sub>-Al<sub>3</sub>Ti during Selective Laser Melting of Nano-TiC/AlSi10Mg Alloy Prepared by Electrostatic Self-Assembly. *Vacuum* **2021**, *188*, 110179. [\[CrossRef\]](#)
67. Tan, Q.; Zhang, J.; Sun, Q.; Fan, Z.; Li, G.; Yin, Y.; Liu, Y.; Zhang, M.X. Inoculation Treatment of an Additively Manufactured 2024 Aluminium Alloy with Titanium Nanoparticles. *Acta Mater.* **2020**, *196*, 1–16. [\[CrossRef\]](#)
68. Zhou, L.; Hyer, H.; Park, S.; Pan, H.; Bai, Y.; Rice, K.P.; Sohn, Y. Microstructure and Mechanical Properties of Zr-Modified Aluminum Alloy 5083 Manufactured by Laser Powder Bed Fusion. *Addit. Manuf.* **2019**, *28*, 485–496. [\[CrossRef\]](#)
69. Xi, L.; Gu, D.; Guo, S.; Wang, R.; Ding, K.; Prashanth, K.G. Grain Refinement in Laser Manufactured Al-Based Composites with TiB<sub>2</sub> Ceramic. *J. Mater. Res. Technol.* **2020**, *9*, 2611–2622. [\[CrossRef\]](#)
70. Wang, Q.Z.; Kang, N.; Lin, X.; EL Mansori, M.; Huang, W.D. High Strength Al-Cu-Mg Based Alloy with Synchronous Improved Tensile Properties and Hot-Cracking Resistance Suitable for Laser Powder Bed Fusion. *J. Mater. Sci. Technol.* **2023**, *141*, 155–170. [\[CrossRef\]](#)
71. Greer, A.L.; Bunn, A.M.; Tronche, A.; Evans, P.V.; Bristow, D.J. Modelling of Inoculation of Metallic Melts: Application to Grain Refinement of Aluminium by Al-Ti-B. *Acta Mater.* **2000**, *48*, 2823–2835. [\[CrossRef\]](#)

**Disclaimer/Publisher’s Note:** The statements, opinions and data contained in all publications are solely those of the individual author(s) and contributor(s) and not of MDPI and/or the editor(s). MDPI and/or the editor(s) disclaim responsibility for any injury to people or property resulting from any ideas, methods, instructions or products referred to in the content.